



HHS Public Access

Author manuscript

IEEE Trans Med Imaging. Author manuscript; available in PMC 2018 August 01.

Published in final edited form as:

IEEE Trans Med Imaging. 2017 August ; 36(8): 1676–1685. doi:10.1109/TMI.2017.2686006.

Constrained Inversion and Spectral Unmixing in Multispectral Optoacoustic Tomography

Lu Ding,

Institute for Biological and Medical Imaging, Helmholtz Center Munich, Neuherberg, Germany and the Faculty of Medicine and the Faculty of Electrical Engineering, Technical University of Munich, Germany

Xosé Luís Deán-Ben,

Institute for Biological and Medical Imaging, Helmholtz Center Munich, Neuherberg, Germany

Neal C. Burton,

iThera Medical GmbH, Munich, Germany

Robert W. Sobol,

Departments of Pharmacology & Chemical Biology and Human Genetics, University of Pittsburgh School of Medicine, Pittsburgh, PA, USA. Current address: University of South Alabama Mitchell Cancer Institute, Mobile, AL, USA

Vasilis Ntziachristos, and

Institute for Biological and Medical Imaging, Helmholtz Center Munich, Neuherberg, Germany and the Faculty of Medicine and the Faculty of Electrical Engineering, Technical University of Munich, Germany

Daniel Razansky

Institute for Biological and Medical Imaging, Helmholtz Center Munich, Neuherberg, Germany and the Faculty of Medicine and the Faculty of Electrical Engineering, Technical University of Munich, Germany

Abstract

Accurate extraction of physical and biochemical parameters from optoacoustic images is often impeded due to the use of unrigorous inversion schemes, incomplete tomographic detection coverage or other experimental factors that cannot be readily accounted for during the image acquisition and reconstruction process. For instance, inaccurate assumptions in the physical forward model may lead to negative optical absorption values in the reconstructed images. Any artifacts present in the single wavelength optoacoustic images can be significantly aggravated when performing a two-step reconstruction consisting in acoustic inversion and spectral unmixing aimed at rendering the distributions of spectrally-distinct absorbers. We investigate a number of algorithmic strategies with non-negativity constraints imposed at the different phases of the reconstruction process. Performance is evaluated in cross-sectional multispectral optoacoustic tomography (MSOT) recordings from tissue-mimicking phantoms and *in vivo* mice embedded with varying concentrations of contrast agents. Additional *in vivo* validation is subsequently

performed with molecular imaging data involving subcutaneous tumors labeled with genetically-expressed iRFP proteins and organ perfusion by optical contrast agents. It is shown that constrained reconstruction is essential for reducing the critical image artifacts associated with inaccurate modeling assumptions. Furthermore, imposing the non-negativity constraint directly on the unmixed distribution of the probe of interest was found to maintain the most robust and accurate reconstruction performance in all experiments.

Index Terms

optoacoustic/photoacoustic tomography; multispectral imaging; spectral unmixing; non-negative constraint

I. Introduction

Multispectral optoacoustic tomography (MSOT) is a hybrid light- and ultrasound-based imaging modality that can resolve the distribution of tissue chromophores and optical contrast agents deep inside highly scattering living organisms [1]–[5]. The basic operational principle consists in identification of absorption spectrum variations in a sequence of optoacoustic images acquired at multiple excitation wavelengths [6]–[8]. The large versatility of optical absorption contrast empowers MSOT with diverse functional and molecular imaging capabilities, often unique among the bio-imaging modalities [9]–[15].

MSOT images representing the distribution of spectrally-distinct chromophores are generally obtained with a two-step procedure. In a first step, optoacoustic tomographic images are reconstructed from the pressure signals generated by absorption of short laser pulses. The signals are recorded at several locations around the imaged object while various inverse algorithms based on back-projection [16], time-reversal [17] or model-based [18]–[21] can be employed for the reconstruction, each offering different trade-offs between the image reconstruction accuracy and computational cost [22]. In the second step, spectral unmixing algorithms are imposed on the images acquired at different excitation wavelengths in order to map the distribution of different absorbing substances present in the tissue. Several spectral processing algorithms based on spectral fitting [6] or blind unmixing [23] have been reported with performance greatly varying among the different approaches. The order of these two steps can be interchanged, i.e., the distribution of a specific substance can alternatively be rendered by multispectral unmixing of the acquired signals and subsequent image reconstruction.

Model-based inversion methods represent arguably the most accurate and versatile approach for both the image reconstruction and unmixing steps in MSOT. They can be adapted to account for the frequency response and geometrical shape of ultrasound sensors [24]–[26] as well as for acoustic mismatch and attenuation [27], [28] and hence significantly enhance image quality. However, applicability of the model-based approach is often limited by lack of exact knowledge of the underlying physical properties of the tissue as well as the illumination and detection geometry, which may lead to inaccurate reconstructions and image artifacts such as negative values with no physical meaning.

For instance, a non-linear spectral model incorporating wavelength-dependent light attenuation effects has been suggested to reduce cross-talk artifacts appearing in the unmixed images obtained with standard linear unmixing [29]. Yet, accurate modeling of light propagation requires prior knowledge of background optical properties, which is very challenging to measure in highly heterogeneous living tissues [30]. Other factors leading to image artifacts are limited detection bandwidth of transducers, limited number of detectors and tomographic coverage, inaccurate modeling assumptions when reducing the problem into two dimensions, inability to accurately account for the spatial light distribution and spectral coloring effect.

To reduce the influence of modeling imperfections, the inversion procedure can be optimized by incorporating constraints or regularization terms, e.g. a non-negative constrained inversion has been shown to render images free of negative absorption values [31]. We have also recently demonstrated that non-negative constrained inversion of a linear two-dimensional optoacoustic tomographic model can further enhance quantitative performance by yielding reconstructed values proportional to the actual absorption coefficient [32].

In this work, we investigate on the impact of non-negative constrained inversion in both the reconstruction and unmixing steps of the MSOT. Linear inverse problems corresponding to reconstruction, unmixing and a combination of both are defined. Performance of the different approaches is subsequently evaluated based on the ability to accurately reconstruct contrast agent distribution in experimental data acquired from tissue-mimicking phantoms and living mice.

II. Theory

In this section, we describe the theoretical basis of MSOT and the simplifications introduced to derive the forward models for the reconstruction and unmixing steps. Based on these forward models, inverse problems where non-negative constraints can be incorporated are defined.

A. Model-based Reconstruction

Time-domain model-based reconstruction algorithms are based on a discrete linear model of the propagation of pressure waves generated by a laser pulse. Assuming thermal and stress confinement conditions and approximating the short-pulsed laser illumination by a Diracs delta in time, the optoacoustic wave equation for a homogeneous acoustic medium can be expressed as [33]

$$\frac{\partial^2 p(\mathbf{r}, t)}{\partial t^2} - c^2 \nabla^2 p(\mathbf{r}, t) = \Gamma H(\mathbf{r}) \frac{\partial \delta(t)}{\partial t}, \quad (1)$$

where Γ is the dimensionless Grüneisen parameter, c is the speed of sound in the medium and $H(\mathbf{r})$ is the amount of energy absorbed in the tissue per unit volume. The solution of (1) is given by the Poisson-type integral via [33]

$$p(\mathbf{r}, t) = \frac{\Gamma}{4\pi c} \frac{\partial}{\partial t} \int_{S'(t)} \frac{H(\mathbf{r}')}{|\mathbf{r} - \mathbf{r}'|} dS'(t). \quad (2)$$

Integration is performed along a spherical surface $S'(t)$ for which $|\mathbf{r} - \mathbf{r}'| = ct$. A cross-sectional acquisition geometry is often assumed with the optoacoustic sources lying in a plane [21], in which case (2) is simplified to

$$p(\mathbf{r}, t) \approx \frac{\Gamma}{4\pi c} \frac{\partial}{\partial t} \int_{L'(t)} \frac{H(\mathbf{r}')}{|\mathbf{r} - \mathbf{r}'|} dL'(t), \quad (3)$$

where $L'(t)$ is a circumference with radius of ct .

A discretization procedure of (2) or (3) leads to a linear forward model expressed as [21]

$$\mathbf{p} = \mathbf{A}\mathbf{h}, \quad (4)$$

where \mathbf{p} is a vector representing pressure signals at all transducer positions, \mathbf{A} is the model matrix with columns representing the time-resolved impulse response from each pixel of the reconstruction region of interest (ROI) to different transducer locations, and \mathbf{h} is a vector containing the absorption at all pixel locations. In model-based reconstruction, the absorption vector is reconstructed from the measured pressure signals \mathbf{p}_m by solving the following least squares problem

$$\hat{\mathbf{h}} = \arg \min_{\mathbf{h}} \|\mathbf{A}\mathbf{h} - \mathbf{p}_m\|_2^2. \quad (5)$$

A regularization term is sometimes incorporated into (5). However, regularization-free results are satisfactory in most cross-sectional optoacoustic tomography reconstructions, given that sufficient angular tomographic coverage is provided by the ultrasound transducers [34].

B. Linear Unmixing

In MSOT, multispectral unmixing is performed to distinguish absorbing substances based on their differential spectral absorption profiles. Assuming a homogeneous Grüneisen parameter in light absorbing regions (mainly vascular structures), the optical absorption h for a certain location \mathbf{r} and a given wavelength λ_j can be expressed in arbitrary units as

$$\begin{aligned}
h(\lambda_i, \mathbf{r}) &= \Phi(\lambda_i, \mathbf{r}) \mu_a(\lambda_i, \mathbf{r}) \\
&= \Phi(\lambda_i, \mathbf{r}) \sum_{j=1}^S (\varepsilon_j(\lambda_i) c_j(\mathbf{r})), \quad (6)
\end{aligned}$$

where $\Phi(\lambda_i, \mathbf{r})$ is the wavelength dependent local light fluence for wavelength i , S is the total number of absorbing substances, $\varepsilon_j(\lambda_i)$ is the molar extinction coefficient of the j -th substance at wavelength λ_i and $c_j(\mathbf{r})$ is its concentration at location \mathbf{r} . The light fluence at different locations in living biological tissues is generally very difficult to measure or estimate without accurate knowledge of the distribution of absorption and scattering coefficients in the entire imaged region. Thereby, a common simplification consists in assuming that the spectral variations of $\Phi(\lambda)$ are negligible with respect to those of $\varepsilon_j(\lambda)$, i.e., $\Phi(\lambda_1, \mathbf{r}) = \Phi(\lambda_2, \mathbf{r}) = \dots = \Phi(\lambda_w, \mathbf{r}) = \tilde{\Phi}(\mathbf{r})$. Let $\tilde{\Phi}$ be the vector containing the light fluence at all pixel locations, $\mathbf{H} = [\mathbf{h}(\lambda_1) \mathbf{h}(\lambda_2) \dots \mathbf{h}(\lambda_w)]$ the wavelength-dependent optical absorption, $\mathbf{C} = [\mathbf{c}_1 \odot \tilde{\Phi} \mathbf{c}_2 \odot \tilde{\Phi} \dots \mathbf{c}_S \odot \tilde{\Phi}]$ having each column being the Hadamard product of the concentration of an absorbing substance and the local light fluence at all pixels, and $\mathbf{E} = [\mathbf{e}_1 \mathbf{e}_2 \dots \mathbf{e}_S]^\top$ representing the molar extinction coefficient of all the absorbing substances. Then, (6) can be expressed in the following simplified matrix relation

$$\mathbf{H} = \mathbf{C}\mathbf{E}. \quad (7)$$

Spectral unmixing of different absorbing substances is performed by solving the following least-square problem [29]

$$\hat{\mathbf{C}} = \arg \min_C \|\mathbf{C}\mathbf{E} - \hat{\mathbf{H}}\|_2^2 \quad (8)$$

with the solution

$$\hat{\mathbf{C}} = \hat{\mathbf{H}}\mathbf{E}^+, \quad (9)$$

where $\hat{\mathbf{H}}$ is the reconstructed optical absorption at all wavelengths and \mathbf{E}^+ is the pseudoinverse of \mathbf{E} . Both the reconstruction and unmixing are linear problems that can be interchanged without affecting the final result. In particular, since $\hat{\mathbf{H}} = \mathbf{A}^+ \mathbf{P}_m$, where $\mathbf{P}_m = [\mathbf{p}_m(\lambda_1) \mathbf{p}_m(\lambda_2) \dots \mathbf{p}_m(\lambda_w)]$, one obtains

$$\hat{\mathbf{C}} = \mathbf{A}^+ \mathbf{P}_m \mathbf{E}^+. \quad (10)$$

Thereby, the unmixed pressure signals

$$\hat{P} = P_m E^+ \quad (11)$$

can be calculated first, while the images of the different absorbers

$$\hat{C} = A^+ \hat{P} \quad (12)$$

only reconstructed at the second step. Note that, since E is a wide matrix with a relatively small number of entries, a lower computational complexity is achieved by first unmixing the signals and subsequently reconstructing the images. Since (10) corresponds to a combined (reconstruction + unmixing) least squares problem expressed as

$$\hat{C} = \arg \min_C \|ACE - P_m\|_2^2, \quad (13)$$

solving the linear reconstruction and multispectral unmixing problems in a separate or in a combined manner would in principle yield equivalent results. However, performance is expected to significantly differ in the case of the non-negative constrained inversion, which introduces non-linearities in the reconstruction process, as described in the following section.

C. Non-negative Constrained Approaches

Non-negative constraints are applicable in any of the inversion problems defined in the previous sections. The constrained least squares problem for tomographic reconstruction is formulated as

$$\hat{h} = \arg \min_{h \geq 0} \|Ah - p_m\|_2^2, \quad (14)$$

and the subsequent non-negative constrained unmixing problem is defined as

$$\hat{C} = \arg \min_{C \geq 0} \|CE - \hat{H}\|_2^2. \quad (15)$$

On the other hand, the combined reconstruction and unmixing inversion procedure can also be formulated as a non-negative constrained inversion problem via

$$\hat{C} = \arg \min_{C \geq 0} \|ACE - P_m\|_2^2. \quad (16)$$

Note that the constraint $C \geq 0$ also implies that $H = CE \geq 0$ since the coefficients in E are non-negative. Note that the non-negative constraint is not applicable for the purpose of signal unmixing prior to reconstructions since the raw recorded optoacoustic signals may generally have physically meaningful negative values. Indeed, the optoacoustic pressure signals are bipolar. For example, the pressure response generated by a spherical object has a characteristic “N” shape with positive and negative pressure values [35]. On the other hand, non-negative constraints can be imposed solely on certain columns of C corresponding to the optical absorbers of interest for the inverse problems in (15) and (16).

As mentioned above, image reconstruction performed with (14) followed by the unmixing step defined in (15) does not generally lead to the same final result as the combined optimization problem in (16).

III. Methods

As discussed in the previous section, non-negativity constraints can be added to the reconstruction and/or unmixing steps. One may also change the order of the reconstruction and unmixing steps or calculate the desired concentrations in a combined manner. Herein, we investigate on the performance of all relevant combinations in terms of quantitiveness and cross-talk artifacts present in the unmixed images. Specifically, the following methods are considered:

- Constrained reconstruction followed by constrained unmixing (CR-CM)
- Constrained reconstruction followed by unconstrained unmixing (CR-UM)
- Unconstrained reconstruction followed by constrained unmixing (UR-CM)
- Unconstrained reconstruction followed by unconstrained unmixing (UR-UM)
- Unconstrained unmixing followed by constrained reconstruction (UM-CR)
- Combined and constrained reconstruction and unmixing (CB1)
- Combined reconstruction and unmixing with a non-negative constraint only imposed on the contrast agent of interest (CB2)

The unconstrained reconstruction problems (UR) defined in (5) were solved with the iterative method LSQR [36], while the unconstrained unmixing problems (UM) defined in (8) were solved directly with the pseudoinverse of E , which can be easily calculated due to its small size. The constrained reconstruction (CR) and the constrained combined problems (CB1 and CB2) were solved using an efficient iterative non-negative least squares method introduced in [32]. On the other hand, the constrained unmixing problems (CM) defined in (15) were solved with the FNNLS method [37], which, due to the small dimensionality of this problem, is more efficient.

Reconstruction performance of all methods was experimentally validated by unmixing the distribution of various chromophores and contrast agents whose extinction (absorption) spectra are depicted in Fig. 1. The absorption spectra for AF750, gold-nanorods (GNR), iRFP [38] and IRDye800CW from spectrophotometer measurements are shown in solid lines and the spectra from MSOT measurements are shown in dashed lines. The MSOT spectra were obtained by imaging phantoms containing the isolated contrast agents at multiple wavelengths and averaging pixel values in the reconstructed optoacoustic images. The measured absorption values were further normalized by the wavelength-dependent energy of the laser source. The MSOT spectra of iRFP and GNR are almost identical to their spectrophotometer spectra while the MSOT spectra of IRDye800CW and AF750 are slightly shifted to the left and the MSOT spectra for AF750 is broadened. The corresponding peak molar extinction coefficients and molecular weight are further listed in TABLE I.

All imaging experiments were done with a commercial small animal multi-spectral optoacoustic tomography scanner (Model: MSOT256-TF, iThera Medical GmbH, Munich, Germany). The scanning system contains a wavelength-tunable (680–950nm) short-pulsed (~ 10 ns) laser. The laser beam is guided through 10 fiber bundles onto the surface of the imaged sample to form a ring-shaped illumination on its surface. The generated optoacoustic responses are captured by a 256-element cylindrically-focused transducer array covering an angle of 270° around the imaged cross-section [39]. During all experiments, the temperature was stabilised at approximately 34°C .

A. Phantom Experiment

In the first experiment, a cylindrical 19 mm diameter agar phantom was imaged containing India ink and Intralipid for mimicking tissue background absorption ($\mu_a = 0.2 \text{ cm}^{-1}$ at 700nm) and scattering properties ($\mu'_s = 10 \text{ cm}^{-1}$) [30]. The acoustic properties of agar are very similar to water. Two 1 mm diameter polyethylene tubings were inserted into the phantom at different depths. AlexaFluor 750 (InvitrogenTM) fluorescent dye at 6 different concentrations (optical densities 0.3, 0.5, 1.1, 1.5, 2.0 and 2.5 as measured with a spectrophotometer) was flushed into and out of the same tubings. Optoacoustic images were recorded with 20 averages at 9 vertical positions of the phantom and at 11 different wavelengths ranging from 700 to 800 nm with 10 nm steps.

B. iRFP-expressing Tumor Cells

To facilitate the mouse tumor studies, we developed a lentiviral vector expressing the phytochrome-based near-infrared fluorescent protein, iRFP [40]. The iRFP [40] complementary DNA was PCR amplified and cloned into the pENTR/D-TOPO plasmid to create the pENTR-iRFP vector via a standard Topo-cloning methodology, as we have described [41]. Once sequence verified, the iRFP was transferred into a Gateway-modified pLVX-IRES-puro vector, as described [42], [43] by TOPO cloning, to generate pLVX-iRFP-IRES-puro. Positive clones were selected and plasmids were extracted with the QIAprep Spin Miniprep Kit (Qiagen). Lentiviral particles were generated by co-transfection of 4 plasmids (The iRFP expression vector pLVX-iRFP-IRES-puro together with pMD2.g (VSVG), pVSV-REV and pMDLg/pRRE) into 293-FT cells using *TransIT-X2*® Dynamic Delivery System (Mirus Bio LLC). The breast cancer cell line MDA-MB-231 (a generous

gift from Dr. Julie Eiseman, University of Pittsburgh) was cultured in RPMI 1640 media supplemented with heat-inactivated FBS (10%) and Gentamycin (10 μ g/ml) at 37°C in humidified chambers with 5% CO₂ and 20% O₂. The MDA-MB-231/iRFP expressing cells were established by overnight transduction of the MDA-MB-231 cells with lentivirus expressing iRFP (pLVX-iRFP-IRES-puro). Transduced cells were then selected for 7–10 days in media supplemented with puromycin (1.5 μ g/ml). The collection and isolation of lentiviral particles and transduction of cells was performed as described previously [44].

C. In Vivo Mouse Experiments

In order to assess the accuracy and sensitivity of the different methods under realistic conditions (including conditions resembling typical molecular imaging studies), data from additional three *in vivo* mouse experiments was further analyzed. All procedures involving animal care and experimentation were conducted according to the guidelines of the Helmholtz Center Munich and the government of Upper Bavaria and complied with German federal and international laws and regulations. All *in vivo* mouse experiments were terminal.

In the first *in vivo* experiment, a polyethylene tubing was inserted into the rectum of a mouse (mouse 1). Ultrasound gel was used as lubricant and for acoustic coupling. Different concentrations of AlexaFluor 750 (optical densities 0.2, 0.5, 1.0, 1.9 and 3.9) as well as GNR (Nanopartz D12-10-780, optical densities 0.3, 0.6, 1.5 and 1.9) were injected into the tubing. For each concentration of the contrast agents, cross-sectional images of the mouse were taken at 10 different positions, from the intestinal region to the legs. At each position, multi-spectral data was recorded with 10 averages at 22 different wavelengths ranging from 690 to 900 nm with 10 nm steps.

For unmixing, the known absorption spectra of oxygenated and deoxygenated hemoglobin were used whereas the spectra of AF750 and GNR were adopted from the results obtained with a blind unmixing procedure [45] in order to compensate for the spectral coloring effects at deep tissue locations [29]. In this scenario, accuracy of the retrieved spectra is ensured due to the local confinement of the imaging agents.

In the second experiment, an 8-week-old female Hsd:Athymic Nude-Foxn1^{nu/nu} mouse was inoculated with 1 million of iRFP-expressing (MDA-MB-231-iRFP) tumor cells in the abdomen region (mouse 2). The tumor was allowed to grow over 10 days reaching an approximate size of 5 mm. No toxicity effects were observed due to the presence of iRFP. Cross-sectional MSOT images were acquired with 10 averages at 680, 690, 700, 715, 730, 760, 800 and 850 nm wavelengths.

In the third *in vivo* experiment, a healthy nude mouse was injected with 20 nmol of IRdye800CW optical contrast agent (LI-COR Biosciences, Lincoln, Nebraska USA) in 100 μ l saline through its tail vein (mouse 3). MSOT images at 715, 730, 760, 780, 800 and 850 nm wavelengths were subsequently taken without averaging approximately 4 min post injection at the kidney region, where the probe accumulates during renal clearance [46].

IV. Results

Results from the phantom experiment are summarized in Fig. 2. Fig. 2a) shows the non-negative constrained reconstruction of the phantom imaged at 740 nm, corresponding to the peak absorption of AF750 in the blindly unmixed spectra. Figs. 2b) and c) display the unmixed distributions of India ink and AF750 for the CR-CM method, i.e., non-negative constrained reconstructions followed by non-negative constrained unmixing.

Clearly, the unmixed distribution of AF750 is confined within the tubings, whilst the amplitude of the deeper insertion is lower due to light fluence attenuation effects. On the other hand, ink is unmixed throughout the phantom as a background component, yet cross-talk artefacts appear inside the tubings. In order to evaluate the accuracy of the AF750 unmixing, the averaged pixel values inside the two tubings (unmixed concentration) obtained with the different methods are plotted in Figs. 2d) and e) as a function of the measured optical density values, which are proportional to the actual concentration. Ideally, the method employed for reconstruction and unmixing should yield unmixed values proportional to the actual concentration of the probe. It can be observed in Figs. 2d) and e) that all methods yield similar results except for UR-CM, for which the relationship between unmixed values and optical density is strongly non-linear for low concentrations of the probe. The data points in Figs. 2d) and e) were fitted to linear functions for each method. Quality of the linear fit is further shown in Fig. 2f). For this particular experiment, no significant differences were observed among the different approaches except for UR-CM, yet the CB2 method exhibits the best linearity.

Results of the *in vivo* mouse experiment (mouse 1) are shown in Fig. 3. Two representative examples for the unmixing of AF750 and GNR are displayed in Figs. 3a)–b) superimposed onto the single wavelength optoacoustic images taken at 800 nm. In particular, Fig. 3a) displays the distribution of AF750 (1.9 OD) in the intestinal region of the mouse unmixed by the CR-CM method while Fig. 3b) shows the distribution of GNR (1.5 OD) for the intestinal/leg area unmixed by the CR-CM method. For the particular slices shown, the probe concentrations inside the tubing obtained with the different methods are further plotted in Figs. 3c) (AF750) and d) (GNR) as a function of the measured optical density of the probes. Much like in the phantom experiments, all methods exhibited a similar performance. In this particular example, the relatively shallow depth of the tubing allows to distinguish relatively low concentrations of the contrast agents, which was not possible for other cross-sections. For a more comprehensive comparison, Figs. 3e)–f) depict the results of a statistical analysis considering 10 different cross-sections of the mouse. Figs. 3e) shows the mean R^2 values for all cross-sections in blue for AF750 and green for GNR and Figs. 3f) shows the standard deviation of the calculated R^2 values for the different methods. It can be seen that most methods again yield similar performance except for UR-CM, which results in a lower R^2 value and high variability of the unmixing performance.

Figs. 4 and 5 show the results of the cross-talk effects evaluation, for which the signal to cross-talk ratio (SCR) was defined as the ratio between the averaged pixel value within the tubings and standard deviation of the background (everywhere else except the tubings). Positive concentrations of AF750 and GNR are illustrated in green and gold respectively

while negative values of both probes are illustrated in the color gray. It can be seen in Fig. 4a) that the images of the unmixed AF750 distribution, which were obtained with the unconstrained methods (CR-UM and UR-UM), contain negative cross-talk artifacts. Fig. 4b) shows the blind spectrum of AF750 used for unmixing. Note that the shape is wider compared to the measured spectrum in Fig. 1 and the peak is slightly shifted to the left. Fig. 4c) shows the respective SCR as a function of the measured optical density of AF750 averaged over the 10 imaged cross-sections. As expected, the SCR is approximately linear with the optical density of the probe. In this particular experiment, the CB2 method yields the best cross-talk performance whereas the UM-CR and UR-UM methods render the strongest cross-talk artifacts. Fig. 5a) displays the unmixed GNR images in the intestinal/leg region rendered using the different methods. Negative cross-talk artifacts are again obtained using the CR-UM and UR-UM methods. Fig. 5b) shows the blind spectrum of GNR. The spectrum is very similar to the measured spectrum in Fig. 1. Fig. 5c) shows the result of the SCR analysis. UR-CM yields the best cross-talk performance while CB1, UM-CR and UR-UM render noisier images of the GNR distribution.

Fig. 6 presents the spectral unmixing results to render the iRFP distribution in mouse 2. Fig. 6a) shows the reconstructed optoacoustic image corresponding to 690 nm (absorption peak of iRFP). Fig. 6b) shows the unmixed iRFP images obtained using the different methods. Here positive concentrations of iRFP are displayed in brown and negative concentrations in green. The tumor can be clearly distinguished in both the single-wavelength and the unmixed images. Note however that the unconstrained methods, namely CR-UM and UR-UM, yield large areas with negative values. Fig. 6c) displays the cross-talk ratios of the unmixed images, calculated as the mean value of the unmixed image inside a region marked in red divided by the standard deviation outside this region. Segmentation of the marked region was done on the single wavelength image using an active contour method [47], [48]. It is readily observed that in this particular experiment the UR-CM method yields the lowest background while the UM-CR and UR-UM methods have the worst cross-talk performance.

Fig. 7 presents the unmixed images of the IRDye800CW dye distribution in the mouse 3 experiment. Here the unmixing results significantly differ among the different methods. Negative artifacts obtained with the CR-UM and UR-UM methods were set to zero for a more convenient representation. From the physiological perspective, the IRDye800CW is expected to clear through kidneys hence mostly accumulate in this area. However, part of the probe remains in the blood circulation, making it difficult to conclude which method renders the most accurate unmixing performance. It is yet clear that the unmixed images rendered with the UM-CR and UR-UM methods contain strong cross-talk artifacts present both inside and outside the mouse, which is consistent with the poor cross-talk performance rendered with these methods in the previous experiments. TABLE II shows the computation time of each method for this data set. Clearly, constrained image reconstruction increases the complexity. The combined methods (CB1 and CB2) are the most time consuming methods while UM-CR is the most efficient method.

V. Discussion and Conclusions

The accuracy of tomographic inversion and spectral unmixing in multispectral optoacoustic tomography (MSOT) depends on a number of experimental and theoretical factors, such as the number, shape and size of the detectors employed, forward modeling imperfections, and discrete sampling issues. This often results in ambiguous reconstructions and appearance of negative values in the images, which have no physical meaning since optical absorption can only be higher or equal than zero. Any artifacts present in the single wavelength optoacoustic images can be significantly aggravated when performing a two-step reconstruction consisting in acoustic inversion and spectral unmixing aimed at rendering the distributions of spectrally-distinct absorbers. In this work, performance of non-negative constrained inversion approaches in multispectral optoacoustic tomography (MSOT) has been evaluated by introducing the constraints at the different image reconstruction and/or probe unmixing steps.

It has been generally established that the constrained inversion is essential for reducing the critical image artifacts associated with inaccurate forward modeling assumptions. Yet, algorithmic sequence has a significant impact on the reconstruction and unmixing performance. Since the combined least squares problem defined in (16) is a convex optimization problem, its solution is the global minimum. Therefore, if we are looking for a solution satisfying $\hat{\mathbf{C}} \geq \mathbf{0}$, the combined problem yields the lowest possible least-squares residual of all approaches. The combined approach is then expected to outperform the other methods if the forward model is accurate. However, modeling imperfections present in practical imaging set-ups may have significant impact on the results, so that the lowest least squares residual may not necessarily guarantee the highest accuracy of the reconstructed images.

Indeed, in practice, imposing the non-negativity constraint directly on the unmixed distribution of the probe of interest (CB2) was found to have the most robust and accurate reconstruction performance in all experiments. Even though the method based on unconstrained reconstruction and subsequent non-negative constrained unmixing (UR-CM) has attained the best SCR in the iRFP experiment, this particular approach is generally not recommendable since it consistently showed an inferior quantitative performance exhibiting a prominent nonlinear dependence between the pixel values in the unmixed image and the actual probe concentration, both in phantom and *in vivo* mouse experiments. On the other hand, more significant crosstalk artifacts were observed for all mouse experiments in the images rendered with the standard unconstrained method (UR-UM) and the method based on unconstrained unmixing followed by constrained reconstruction (UM-CR), which suggests that these approaches provide a lower sensitivity in detecting optical probes.

In view of both phantom and *in vivo* imaging results, the combined non-negative constrained method has arguably achieved the best results in terms of artifact-free spectral unmixing, also yielding the lowest least-squares residual during the inversion and unmixing process. The combined approach is further expected to provide an efficient platform for further improving the forward model accuracy by e.g. incorporating the wavelength-dependent light fluence distribution into the model. Estimation of light fluence variations is very challenging

since the exact optical properties of heterogeneous living tissues cannot be easily estimated or measured [49]. Nevertheless, methods based on e.g. extraction of low spatial frequency components from the images [50], analyzing signal variations by means of photoswitchable probes [51] or multi-modal imaging approaches [52] have shown promise in delivering reasonably good estimates on the light fluence distribution. Note that the current work was aimed at unmixing the distribution of spatially-confined contrast agents, in which case the agent's contribution to the optical attenuation and spectral coloring is assumed to be insignificant. As a result, the utilized blind unmixing approach can effectively account for the spectral coloring effects when the unmixed chromophore is assumed to be sparsely distributed in the sample. Yet, accurately accounting for the wavelength-dependent light fluence distribution may turn important when instead aiming at mapping the blood oxygen saturation levels. The absorption spectra of hemoglobin are distorted (colored) at deeper locations, resulting in errors in the estimated oxygen saturation if the theoretical spectra are considered for unmixing. In this regard, the proposed non-negative constrained framework can be potentially extended by incorporating more sophisticated methods accounting for the wavelength dependence attenuation in the light fluence model [53]. It is important to note that the results showcased in this work correspond to a crosssectional acquisition geometry, for which a two-dimensional optoacoustic model was assumed. While being a practical imaging configuration widely employed in small-animal optoacoustic imaging studies, three-dimensional acquisition geometries are generally expected to provide more accurate estimates on the actual volumetric (three-dimensional) distribution of probes [5], [54]. In this case, a three-dimensional model-based reconstruction algorithm is required [20], [31], which can further be optimized by accounting for the exact three-dimensional shape of the individual ultrasound detectors [26]. A study on the influence of non-negative constraints in three-dimensional model-based reconstructions accounting for the actual shape of the sensors is aimed at in our future investigations.

In conclusion, the impact of non-negative constraints in inversion problems corresponding to reconstruction and unmixing in MSOT was investigated. The newly proposed combined reconstruction and unmixing method with a non-negative constraint imposed directly on the distribution of the probe (CB2) of interest appears to be an efficient approach with robust performance in all phantom and mouse experiments. The proposed method further establishes a convenient framework to account for a variety of additional factors affecting the final images.

Acknowledgments

The authors acknowledge grant support from the European Research Council under Consolidator Grant ERC-2015-CoG- 682379 (D. R.), Human Frontier Science Program (HFSP) Grant RGY0070/2016 (D. R.), SFB1123 (V. N.), NIH grant R01CA148629 and the Abraham A. Mitchell Distinguished Investigator fund (R. W. S.). RWS is a scientific consultant for Trevigen, Inc. and an Abraham A. Mitchell Distinguished Investigator. The authors also acknowledge assistance in cell culture and cell purification from T. C. P. Sardella.

References

1. Razansky D, Distel M, Vinegoni C, Ma R, Perrimon N, Köster RW, Ntziachristos V. Multispectral opto-acoustic tomography of deep-seated fluorescent proteins in vivo. *Nature Photonics*. 2009; 3(7): 412–417.

2. Yao J, Wang LV. Photoacoustic tomography: fundamentals, advances and prospects. *Contrast media & molecular imaging*. 2011; 6(5):332–345. [PubMed: 22025335]
3. Jeon M, Kim J, Kim C. Multiplane spectroscopic whole-body photoacoustic imaging of small animals in vivo. *Medical & biological engineering & computing*. 2016; 54(2–3):283–294. [PubMed: 25115270]
4. Nie L, Chen X. Structural and functional photoacoustic molecular tomography aided by emerging contrast agents. *Chemical Society Reviews*. 2014; 43(20):7132–7170. [PubMed: 24967718]
5. Deán-Ben XL, Razansky D. Adding fifth dimension to optoacoustic imaging: volumetric time-resolved spectrally enriched tomography. *Light: Science & Applications*. 2014; 3(1):e137.
6. Cox B, Arridge S, Beard P. Estimating chromophore distributions from multiwavelength photoacoustic images. *JOSA A*. 2009; 26(2):443–455. [PubMed: 19183699]
7. Luke GP, Nam SY, Emelianov SY. Optical wavelength selection for improved spectroscopic photoacoustic imaging. *Photoacoustics*. 2013; 1(2):36–42. [PubMed: 25302148]
8. Tzoumas S, Delioliannis NC, Morscher S, Ntziachristos V. Unmixing molecular agents from absorbing tissue in multispectral optoacoustic tomography. *IEEE transactions on medical imaging*. 2014; 33(1):48–60. [PubMed: 24001986]
9. Yao J, Xia J, Maslov KI, Nasiriavanaki M, Tsytsarev V, Demchenko AV, Wang LV. Noninvasive photoacoustic computed tomography of mouse brain metabolism in vivo. *Neuroimage*. 2013; 64:257–266. [PubMed: 22940116]
10. Ermolayev V, Dean-Ben XL, Mandal S, Ntziachristos V, Razansky D. Simultaneous visualization of tumour oxygenation, neovascularization and contrast agent perfusion by real-time three-dimensional optoacoustic tomography. *European radiology*. 2016; 26(6):1843–1851. [PubMed: 26334513]
11. Stiel AC, Deán-Ben XL, Jiang Y, Ntziachristos V, Razansky D, Westmeyer GG. High-contrast imaging of reversibly switchable fluorescent proteins via temporally unmixed multispectral optoacoustic tomography. *Optics letters*. 2015; 40(3):367–370. [PubMed: 25680049]
12. Bohndiek SE, Sasportas LS, Machtaler S, Jokerst JV, Hori S, Gambhir SS. Photoacoustic tomography detects early vessel regression and normalization during ovarian tumor response to the antiangiogenic therapy trebananib. *Journal of Nuclear Medicine*. 2015; 56(12):1942–1947. [PubMed: 26315834]
13. Schwarz M, Buehler A, Aguirre J, Ntziachristos V. Three-dimensional multispectral optoacoustic mesoscopy reveals melanin and blood oxygenation in human skin in vivo. *Journal of biophotonics*. 2016; 9(1–2):55–60. [PubMed: 26530688]
14. Jathoul AP, Laufer J, Ogunlade O, Treeby B, Cox B, Zhang E, Johnson P, Pizzey AR, Philip B, Marafioti T, et al. Deep in vivo photoacoustic imaging of mammalian tissues using a tyrosinase-based genetic reporter. *Nature Photonics*. 2015
15. Gottschalk S, Fehm TF, Deán-Ben XL, Razansky D. Non-invasive real-time visualization of multiple cerebral hemodynamic parameters in whole mouse brains using five-dimensional optoacoustic tomography. *Journal of Cerebral Blood Flow & Metabolism*. 2015; 35(4):531–535. [PubMed: 25586142]
16. Xu M, Wang LV. Universal back-projection algorithm for photoacoustic computed tomography. *Physical Review E*. 2005; 71(1):016706.
17. Hristova Y, Kuchment P, Nguyen L. Reconstruction and time reversal in thermoacoustic tomography in acoustically homogeneous and inhomogeneous media. *Inverse Problems*. 2008; 24(5):055006.
18. Paltauf G, Viator J, Prah S, Jacques S. Iterative reconstruction algorithm for optoacoustic imaging. *The Journal of the Acoustical Society of America*. 2002; 112(4):1536–1544. [PubMed: 12398460]
19. Ephrat P, Keenliside L, Seabrook A, Prato FS, Carson JJ. Three-dimensional photoacoustic imaging by sparse-array detection and iterative image reconstruction. *Journal of Biomedical Optics*. 2008; 13(5):054 052–054 052.
20. Dean-Ben XL, Buehler A, Ntziachristos V, Razansky D. Accurate model-based reconstruction algorithm for three-dimensional optoacoustic tomography. *IEEE Transactions on Medical Imaging*. 2012; 31(10):1922–1928. [PubMed: 23033065]

21. Rosenthal A, Razansky D, Ntziachristos V. Fast semi-analytical model-based acoustic inversion for quantitative optoacoustic tomography. *IEEE transactions on medical imaging*. 2010; 29(6):1275–1285. [PubMed: 20304725]
22. Rosenthal A, Ntziachristos V, Razansky D. Acoustic inversion in optoacoustic tomography: A review. *Current medical imaging reviews*. 2013; 9(4):318–336. [PubMed: 24772060]
23. Glatz J, Deliolanis NC, Buehler A, Razansky D, Ntziachristos V. Blind source unmixing in multi-spectral optoacoustic tomography. *Optics express*. 2011; 19(4):3175–3184. [PubMed: 21369139]
24. Rosenthal A, Ntziachristos V, Razansky D. Model-based optoacoustic inversion with arbitrary-shape detectors. *Medical physics*. 2011; 38(7):4285–4295. [PubMed: 21859030]
25. Mitsuhashi K, Wang K, Anastasio MA. Investigation of the far-field approximation for modeling a transducer's spatial impulse response in photoacoustic computed tomography. *Photoacoustics*. 2014; 2(1):21–32. [PubMed: 24579061]
26. Queirós D, Déan-Ben XL, Buehler A, Razansky D, Rosenthal A, Ntziachristos V. Modeling the shape of cylindrically focused transducers in three-dimensional optoacoustic tomography. *Journal of biomedical optics*. 2013; 18(7):076 014–076 014.
27. Deán-Ben XL, Ma R, Rosenthal A, Ntziachristos V, Razansky D. Weighted model-based optoacoustic reconstruction in acoustic scattering media. *Physics in medicine and biology*. 2013; 58(16):5555. [PubMed: 23892587]
28. Huang C, Nie L, Schoonover RW, Wang LV, Anastasio MA. Photoacoustic computed tomography correcting for heterogeneity and attenuation. *Journal of biomedical optics*. 2012; 17(6):0 612 111–0 612 115.
29. Cox B, Laufer JG, Arridge SR, Beard PC. Quantitative spectroscopic photoacoustic imaging: a review. *Journal of biomedical optics*. 2012; 17(6):0 612 021–06 120 222.
30. Jacques SL. Optical properties of biological tissues: a review. *Physics in medicine and biology*. 2013; 58(11):R37. [PubMed: 23666068]
31. Wang K, Su R, Oraevsky AA, Anastasio MA. Investigation of iterative image reconstruction in three-dimensional optoacoustic tomography. *Physics in medicine and biology*. 2012; 57(17):5399. [PubMed: 22864062]
32. Ding L, Deán-Ben XL, Lutzweiler C, Razansky D, Ntziachristos V. Efficient non-negative constrained model-based inversion in optoacoustic tomography. *Physics in medicine and biology*. 2015; 60(17):6733. [PubMed: 26295866]
33. Cox B, Kara S, Arridge S, Beard P. k-space propagation models for acoustically heterogeneous media: Application to biomedical photoacoustics. *The Journal of the Acoustical Society of America*. 2007; 121(6):3453–3464. [PubMed: 17552697]
34. Buehler A, Rosenthal A, Jetzfellner T, Dima A, Razansky D, Ntziachristos V. Model-based optoacoustic inversions with incomplete projection data. *Medical physics*. 2011; 38(3):1694–1704. [PubMed: 21520882]
35. Wang, LV., Wu, H-i. *Biomedical optics: principles and imaging*. John Wiley & Sons; 2012.
36. Paige CC, Saunders MA. Lsqr: An algorithm for sparse linear equations and sparse least squares. *ACM transactions on mathematical software*. 1982; 8(1):43–71.
37. Bro R, De Jong S. A fast non-negativity-constrained least squares algorithm. *Journal of chemometrics*. 1997; 11(5):393–401.
38. Shcherbakova DM, Verkhusha VV. Near-infrared fluorescent proteins for multicolor in vivo imaging. *Nature methods*. 2013; 10(8):751–754. [PubMed: 23770755]
39. Razansky D, Buehler A, Ntziachristos V. Volumetric real-time multispectral optoacoustic tomography of biomarkers. *Nature protocols*. 2011; 6(8):1121–1129. [PubMed: 21738125]
40. Filonov GS, Piatkevich KD, Ting LM, Zhang J, Kim K, Verkhusha VV. Bright and stable near-infrared fluorescent protein for in vivo imaging. *Nature biotechnology*. 2011; 29(8):757–761.
41. Trivedi RN, Wang X-h, Jelezcova E, Goellner EM, Tang J-b, Sobol RW. Human methyl purine dna glycosylase and dna polymerase β expression collectively predict sensitivity to temozolomide. *Molecular Pharmacology*. 2008; 74(2):505–516. [PubMed: 18477668]
42. Fang Q, Inanc B, Schamus S, Wang X-h, Wei L, Brown AR, Svilar D, Sugrue KF, Goellner EM, Zeng X, et al. Hsp90 regulates dna repair via the interaction between xrcc1 and dna polymerase β . *Nature communications*. 2014; 5

43. Tang, J-b, Goellner, EM., Wang, X-h, Trivedi, RN., St Croix, CM., Jelezcova, E., Svilar, D., Brown, AR., Sobol, RW. Bioenergetic metabolites regulate base excision repair-dependent cell death in response to dna damage. *Molecular Cancer Research*. 2010; 8(1):67–79. [PubMed: 20068071]
44. Fouquerel E, Goellner EM, Yu Z, Gagne JP, de Moura MB, Feinstein T, Wheeler D, Redpath P, Li J, Romero G, et al. Artd1/parp1 negatively regulates glycolysis by inhibiting hexokinase 1 independent of nad+ depletion. *Cell reports*. 2014; 8(6):1819–1831. [PubMed: 25220464]
45. Deán-Ben XL, Deliolanis NC, Ntziachristos V, Razansky D. Fast unmixing of multispectral optoacoustic data with vertex component analysis. *Optics and Lasers in Engineering*. 2014; 58:119–125.
46. Scarfe L, Rak-Raszewska A, Geraci S, Darssan D, Sharkey J, Huang J, Burton NC, Mason D, Ranjzad P, Kenny S, et al. Measures of kidney function by minimally invasive techniques correlate with histological glomerular damage in scid mice with adriamycin-induced nephropathy. *Scientific reports*. 2015; 5
47. Mandal S, Deán-Ben XL, Razansky D. Visual quality enhancement in multispectral optoacoustic tomography using active contour segmentation priors. 2015 arXiv preprint arXiv:1510.08174.
48. Chan TF, Vese LA. Active contours without edges. *IEEE Transactions on image processing*. 2001; 10(2):266–277. [PubMed: 18249617]
49. Lutzweiler C, Razansky D. Optoacoustic imaging and tomography: reconstruction approaches and outstanding challenges in image performance and quantification. *Sensors*. 2013; 13(6):7345–7384. [PubMed: 23736854]
50. Rosenthal A, Razansky D, Ntziachristos V. Quantitative optoacoustic signal extraction using sparse signal representation. *IEEE transactions on medical imaging*. 2009; 28(12):1997–2006. [PubMed: 19628454]
51. Dean-Ben, XL., Stiel, AC., Jiang, Y., Ntziachristos, V., Westmeyer, GG., Razansky, D. Optical Tomography and Spectroscopy. *Optical Society of America*; 2016. Light fluence estimation by imaging photoswitchable probes with temporally unmixed multispectral optoacoustic tomography; p. OTu2A-6
52. Bauer AQ, Nothdurft RE, Erpelding TN, Wang LV, Culver JP. Quantitative photoacoustic imaging: correcting for heterogeneous light fluence distributions using diffuse optical tomography. *Journal of Biomedical Optics*. 2011; 16(9):096 016–096 016.
53. Tzoumas S, Nunes A, Olefir I, Stangl S, Symvoulidis P, Glasl S, Bayer C, Multhoff G, Ntziachristos V. Eigenspectra optoacoustic tomography achieves quantitative blood oxygenation imaging deep in tissues. *Nature Communications*. 2016; 7:12121.
54. Deán-Ben XL, Razansky D. Portable spherical array probe for volumetric real-time optoacoustic imaging at centimeter-scale depths. *Optics express*. 2013; 21(23):28 062–28 071.

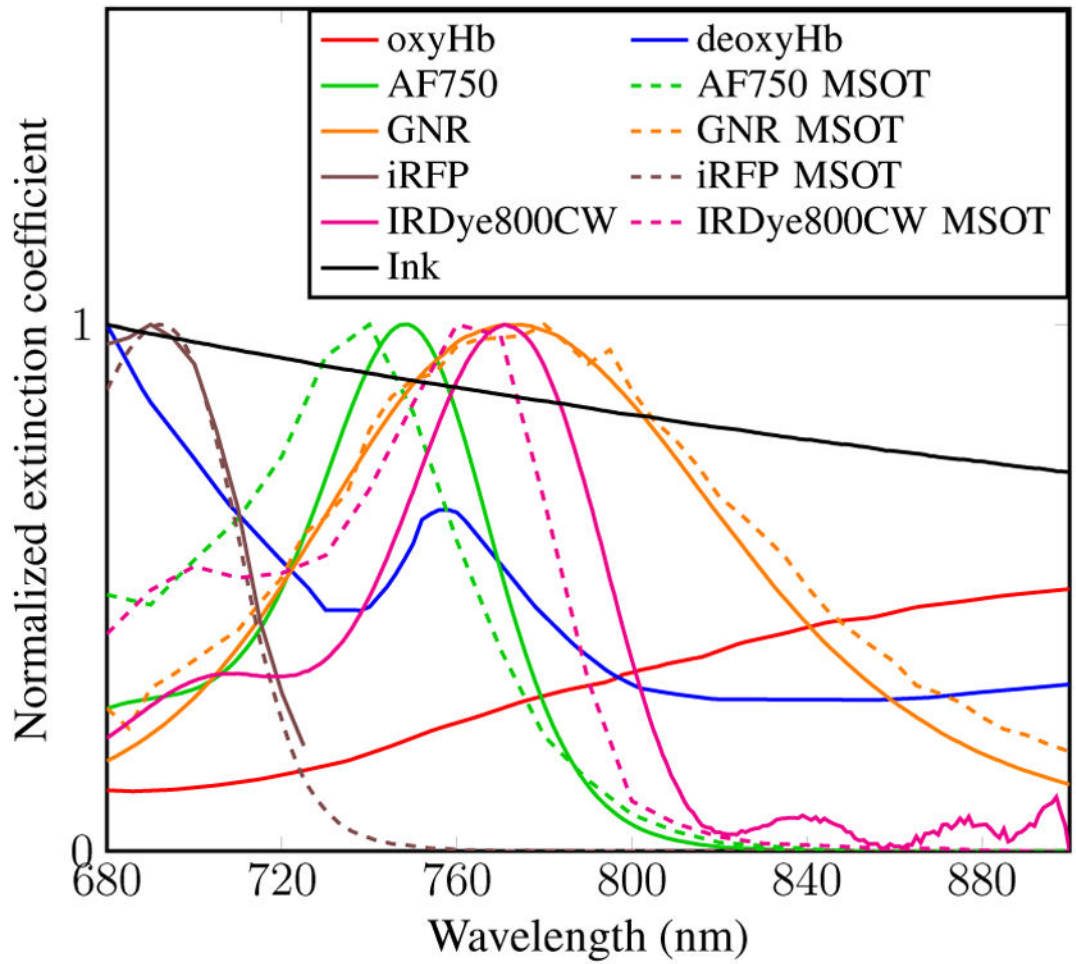


Fig. 1. Normalized extinction (absorption) spectra of the different intrinsic tissue chromophores and optical contrast agents considered in this study.

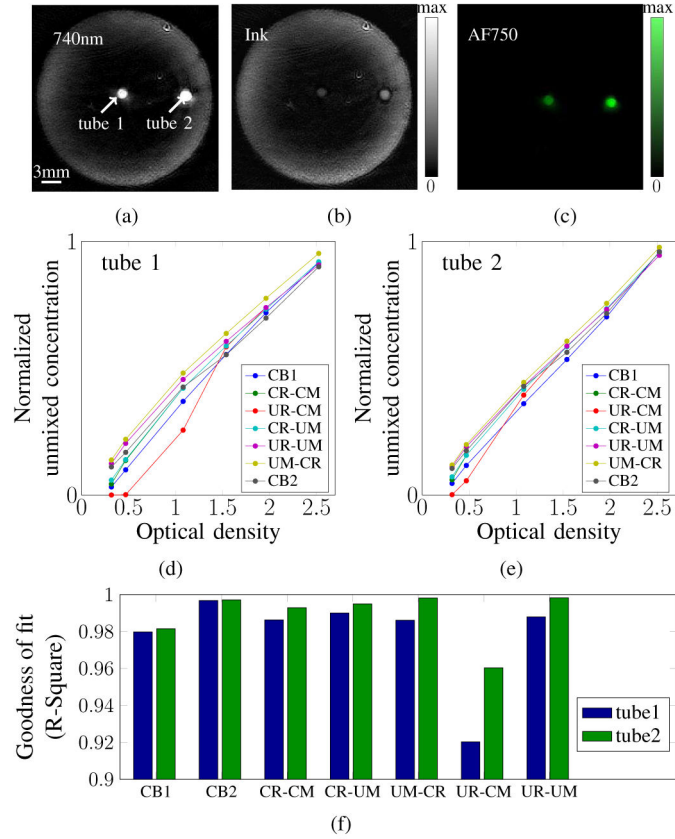


Fig. 2. Unmixing results for the phantom with background ink absorption and two insertions (tubes) containing AF750 dye. a) Optoacoustic image acquired at 740 nm with 2.5 OD of AF750 insertion. b) Unmixed image corresponding to the ink component obtained with the CR-CM method. c) Unmixed image corresponding to the AF750 component obtained with the CR-CM method. d)–e) Normalized unmixing concentration (pixel values of the unmixed image) within the tubes as a function of the optical density of AF750. f) The R^2 values, representing quality of the linear fit in d) and e).

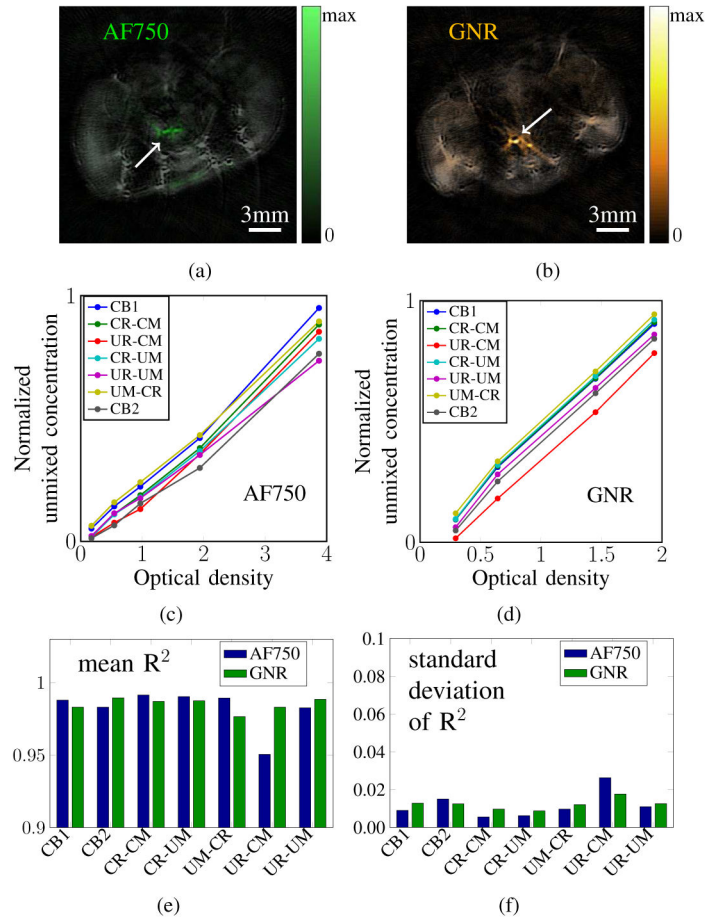


Fig. 3. Unmixing results for the *in vivo* (mouse 1) experiment. a) Unmixed distribution of AF750 obtained with the CR-CM method. b) Unmixed distribution of GNR obtained with the CR-CM method. c)–d) Unmixed optoacoustic signal within the tubes as a function of the optical density of AF750 and GNR, respectively, normalized to the maximum value for the corresponding slices. e)–f) Statistical analysis of the linear fit of the curves in c)–d). All 10 imaged cross-sections were taken into account.

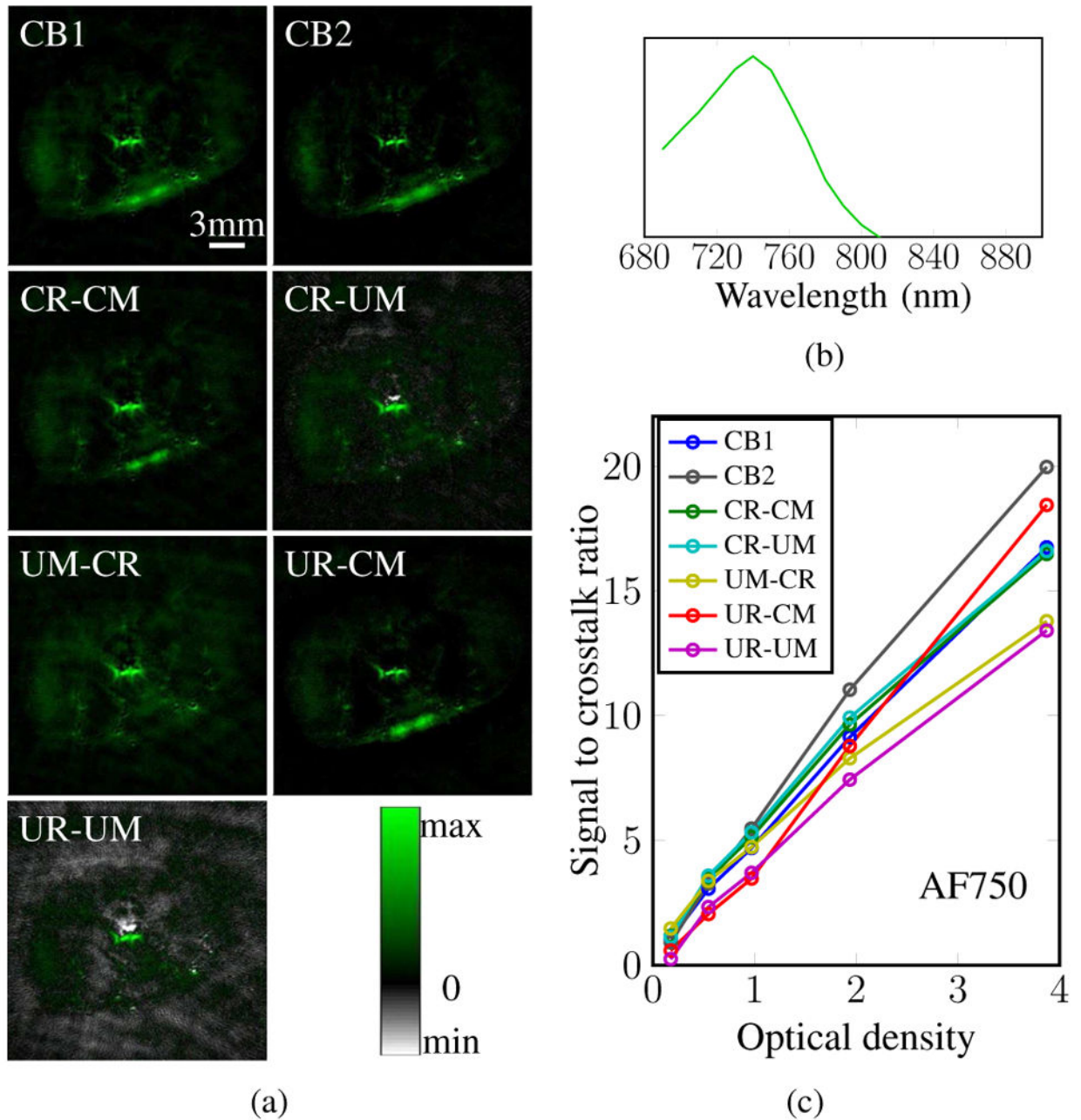


Fig. 4. Cross-talk artifacts evaluation for the AF750 probe unmixing in mouse 1. a) Unmixed distribution of AF750 (1.9 OD) for an intestinal region slice using the different reconstruction and unmixing methods. b) Blind spectrum of AF750 used for unmixing. c) Signal to cross-talk ratios as a function of the optical density of AF750 averaged over all 10 imaged cross-sections.

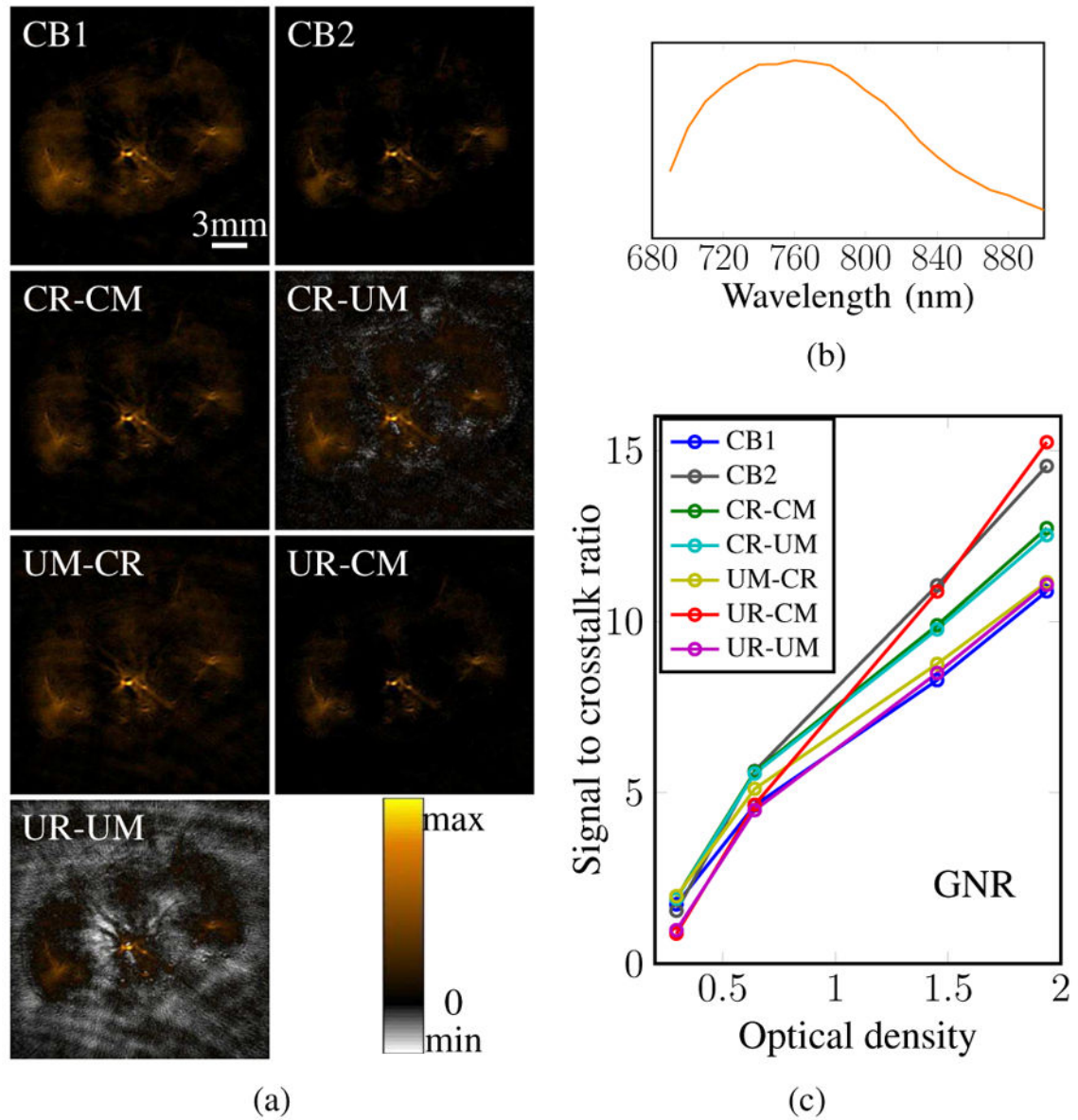


Fig. 5. Cross-talk artifacts evaluation for the GNR unmixing in mouse 1. a) Unmixed distribution of GNR (1.5 OD) for an intestinal/leg region. b) Blind spectrum of GNR used for unmixing. c) Signal to cross-talk ratios as a function of the optical density of GNR averaged over all 10 imaged cross-sections.

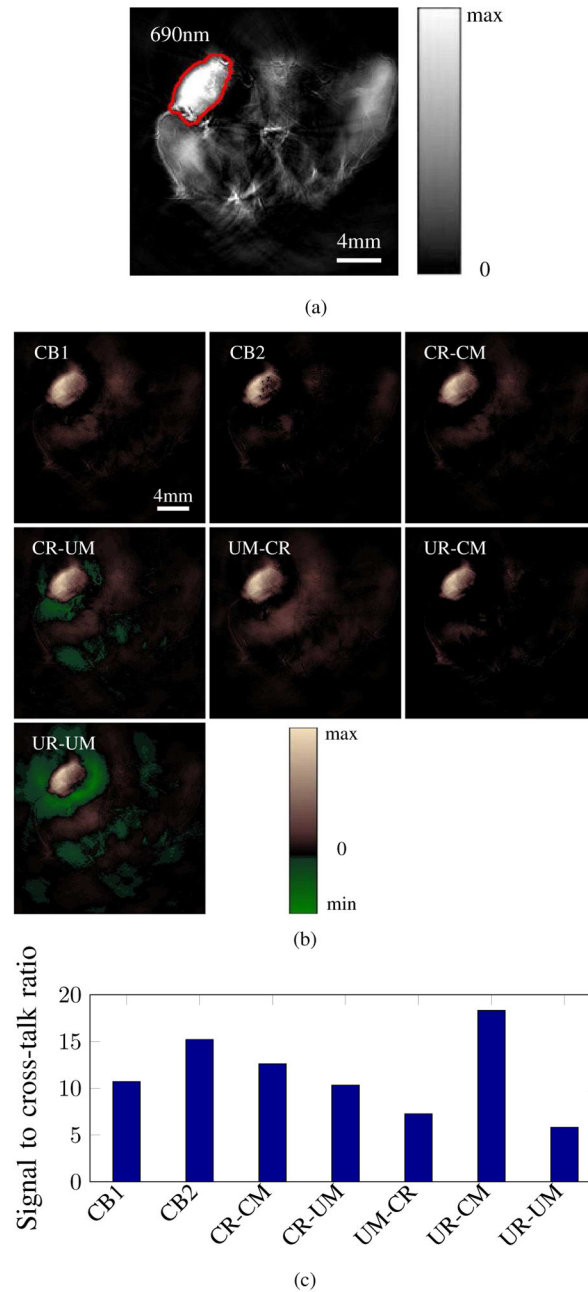


Fig. 6. Results of the *in vivo* iRFP unmixing experiment in mouse 2. a) Single wavelength optoacoustic image (gray scale) acquired at 690 nm. b) Unmixed distributions of iRFP obtained using different methods (brown-green scale). c) Cross-talk performance of different methods - the unmixed iRFP signal is assumed to be confined within the red region marked in a).

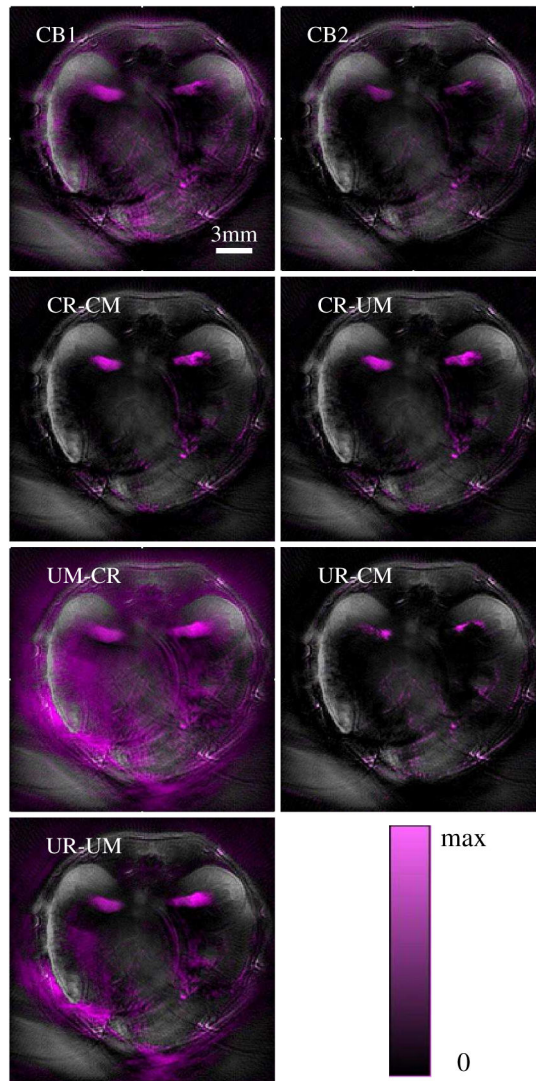


Fig. 7. Unmixed distributions of IRDye800CW obtained using the different non-negative constraints. The probe distribution (represented on a purple scale) is superimposed onto the single wavelength optoacoustic images acquired at 850 nm showing accumulation in the renal medulla while clearing through kidneys.

TABLE I

Peak Molar Extinction Coefficient and Molecular Weight of the Intrinsic Tissue Chromophores and Optical Contrast Agents.

	Peak Molar Ext. ($M^{-1}cm^{-1}$)	Wavelength (nm)	Molecular Weight (g/mole)
oxyHb	1198	900	64500
deoxyHb	2407.92	680	64500
AF750	$2.9 \cdot 10^5$	749	~ 1300
GNR	$8.92 \cdot 10^8$	760	~ $3.1 \cdot 10^7$
iRFP	$8.5 \cdot 10^4$	692	35000
IRDye800CW	$2.4 \cdot 10^5$	774	1091.11

Author Manuscript

Author Manuscript

Author Manuscript

Author Manuscript

TABLE II

Computation Time of Different Methods for the in vivo IRDye800CW experiment.

Method	Computation time
CB1	77s
CB2	120s
CR-CM	42s + 4.6s
CR-UM	42s + 0.005s
UM-CR	0.01s + 22.5s
UR-CM	13.2s + 2.4s
UR-UM	13.2s + 0.005s

Author Manuscript

Author Manuscript

Author Manuscript

Author Manuscript